The effect of hydrodynamics on the bending failure of level ice

Keijdener, Chris; Hendrikse, Hayo; Metrikine, Andrei

Important note
To cite this publication, please use the final published version (if applicable).
Please check the document version above.

The effect of hydrodynamics on the bending failure of level ice

Chris Keijdener[a,b,*], Hayo Hendrikse[a,b], Andrei Metrikine[a,b]

[a] *Delft University of Technology, Stevinweg 1, 2628CN Delft, Netherlands*
[b] *Department of Civil and Transport Engineering, SAMCoT, NTNU, NO-7491 Trondheim, Norway*

A B S T R A C T

In this paper, the bending failure of level ice caused by the interaction with a downward sloping structure is studied in 2D. The focus is on the effect of hydrodynamics on the interaction. This study is done by comparing the predictions of a model that includes both hydrostatics and hydrodynamics with one that only includes hydrostatics.

For both models, the ice is modeled as a semi-infinite Kirchhoff-Love plate that is assumed to float on an infinitely wide fluid layer of finite depth. The fluid pressure exerted on the ice is governed by the nonlinear Bernoulli equation. The ice moves towards the structure, impacts with its downward sloping hull, slides down the structure and ultimately fails in downward bending. Validation of this model shows good agreement with experimental data.

It is shown that the nonlinear term in the Bernoulli equation has a negligible effect on the interaction and can be ignored. The effect of hydrodynamics can thus be attributed to the linear part of the hydrodynamic pressure. The effect of the rotational inertia of the ice and axial compression is negligible as well. At low velocities, ice fails in a quasi-static manner, while at higher velocities, the failure takes place shortly after the contact initiation. The transition between these two regimes is marked by a transition velocity that is significantly lower for the hydrodynamic model than for the hydrostatic one. Because of this, it is not desirable to use the hydrostatic model for velocities above the transition velocity.

1. Introduction

The Arctic Region is expected to contain 22% of the worlds unexplored hydrocarbon reserves and of these reserves, 84% is expected to be located offshore (Bird et al., 2008). For the extraction of offshore hydrocarbons, both bottom-founded and floating production platforms are commonly used. Bottom-founded platforms are limited to shallow waters, making floating platforms essential in gaining access to the majority of the Arctic's hydrocarbons. For the safe and sustainable extraction of hydrocarbons in the Arctic, it is therefore paramount to both understand and be able to predict ice structure interaction (ISI).

When modeling ISI, assumptions have to be made regarding the fluid. Most modern ISI models tend to focus on the contact-based interaction between the ice floes and the structure and chose to ignore most hydrodynamic effects (Paavilainen et al., 2009; Su et al., 2010; Lubbad and Loset, 2011; Konno et al., 2013; Lu et al., 2014; Alawneh et al., 2015; Metrikin et al., 2015; Sayed et al., 2015). The majority of these models capture hydrodynamics (HD) in an effective manner using a frequency independent added mass coefficient. This approach, however, appears to be insufficiently accurate in capturing hydrodynamic

effects (Dempsey and Zhao, 1993; Zhao and Dempsey, 1996).

In the closely related field of ice-ship interaction, HD has been shown to be a key component of ISI. This field studies the response of ships moving through ice-infested water. A major contribution was made by Valanto (1992) who, through a combination of numerical and experimental work, identified that HD greatly affects both the contact load and the breaking length of the ice and that it is a key factor in their velocity dependence.

Despite this seminal work, there are still open questions regarding the effect of HD on ISI. Firstly, the pressure of an ideal, incompressible fluid is given by the Bernoulli equation. This equation contains three terms of which two are responsible for the HD effects. However, it is still unclear whether both terms are important for ISI. Likewise, the importance of various other factors, such as rotational inertia and axial compression, has not been studied before. Therefore, the first goal of this paper is to determine the factors of influence for ISI. Secondly, it is unclear how the various factors form a balance and how HD affects this balance. Studying the balance is the second goal of this paper. Thirdly, no detailed study has been done on the relation between the contact load and the breaking length and how HD affects this relation.

Elucidating this relation is the third goal of this paper. Lastly, as most ISI models are still limited to hydrostatics, it is important to study the limitations of hydrostatic models. Studying these limitations is the last goal of this paper.

To achieve these four goals, a semi-analytical model is proposed that includes the complete nonlinear Bernoulli equation for the description of the fluid pressure. This model is introduced in the next section and validated in Section 3. The factors of influence for ISI are determined in Subsection 4.1. Thereafter, these factors are studied to determine how they form a balance of forces in the ice in Subsection 4.2. Next, the influence of HD on the relation between contact load and breaking length is studied in Section 4.3. In order to compare the predictions of the hydrodynamic model with those of the hydrostatic model, all computations are done using both models. Results from the comparison are used to identify the limitations of hydrostatic models in Subsection 4.4. All studies are done for a range of ice velocities. The sensitivity of the results to the choice of model parameters is assessed in Section 5. A discussion follows in Section 6 and conclusions are given in Section 7.

2. Model description

To analyze the effects of HD on the ISI, a 2D semi-analytical model is employed that is described in this section. The model is depicted in Fig. 1.

The ice, located at $x \leq 0$, is modeled as a semi-infinite Kirchhoff-Love plate that includes rotational inertia and axial compression. The ice floats on an infinitely wide fluid layer with depth H. As no ice is present at $x > 0$, the fluid has a free surface in this region.

It is assumed that the ice moves towards the structure with a constant forward velocity V_{ice}. The structure is assumed to be rigid and immovable. For the interaction with the fluid, the geometry of the structure is ignored. Therefore, the structure does not affect the mathematical model of the fluid. The validity of this assumption is assessed in Section 5.2. For the interaction with the ice, the structure is reduced to a line passing through $x = z = 0$ with a hull angle θ with respect to the x-axis, see Fig. 1. As the ice moves forward, it interacts with the structure. This interaction generates loads on the edge of the ice, causing it to slide down along the structure until it fails in bending.

In the next subsection, the mathematical model is described. Following this, the solution method is explained.

2.1. Mathematical model

2.1.1. Fluid

The fluid is assumed to be incompressible, inviscid and irrotational and so is governed by the Laplace equation:

$$\Delta \dot{\phi}(x,z,t) = 0 \quad \forall \ x \in (-\infty,\infty) \cap z \in (-H,0) \tag{1}$$

where $\phi(x, z, t)$ is the displacement potential of the fluid (Jensen et al., 2011), the dot denotes derivatives with respect to time, round
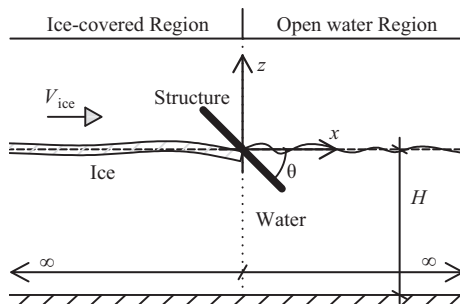
brackets denote an open interval while square brackets, in the equations to follow, denote a closed interval. The boundary condition at the seabed prevents penetration of the fluid into the seabed:

$$\frac{\partial \phi(x,-H,t)}{\partial z} = 0 \quad \forall \ x \in (-\infty,\infty) \tag{2}$$

The fluid pressure is calculated according to the Bernoulli equation for unsteady, imcompressible potential flow (Stoker, 1992):

$$p(x,z,t) = -\rho_w \left(\ddot{\phi} + \frac{1}{2}v^2 + g\frac{\partial\phi}{\partial z} \right) \tag{3}$$

where $p(x, z, t)$ is the fluid pressure, ρ_w is the fluid density, g is the gravitational constant and the squared fluid speed is given by $v^2 = \left(\frac{\partial\phi}{\partial x}\right)^2 + \left(\frac{\partial\phi}{\partial z}\right)^2$. The fluid pressure is thus composed of three terms. From left to right these three terms will be referred to as the linear hydrodynamic, nonlinear hydrodynamic and hydrostatic pressure, abbreviated as p_{HD}, p_{NLHD} and p_{HS} respectively. The first two terms together comprise the hydrodynamic effect and by disabling them a model with only hydrostatic effects is obtained. For $x \leq 0$, the ice is present at the surface and so the surface boundary condition of the fluid contains the equation of motion of the plate. For $x > 0$, no ice is present and so the pressure release condition is imposed. As the draft of the ice can be ignored, as was shown by Williams and Squire (2008), the boundary condition of the fluid can be formulated at $z = 0$:

$$(x,0,t) = \begin{cases} \rho_i h\ddot{w} + \rho_i \frac{h^3}{12}\ddot{w}'' + \frac{E}{1-\nu^2}\frac{h^3}{12}w'''' \\ +F_{ct,x}(t,w,w',\dot{w},\dot{w}')w'' & \forall \ x \in (-\infty,0) \\ 0 & \forall \ x \in (0,\infty) \end{cases} \tag{4}$$

where ρ_i is the density of the ice, h its thickness, $w(x, t)$ its vertical displacement, E its Young's modulus, ν its Poisson ratio and the prime denotes a spatial derivative. Note that the plate's bending stiffness, $Eh^3/12$, aims to capture the bending behavior of level ice, including any variation of temperature, stiffness or other property across its thickness, in an effective manner, similar to what is done for functionally graded materials. This approach is assumed to be valid given that only very long wavelengths are excited in ice. The axial compression in the ice is assumed to be constant in space and equal to the horizontal component of the contact force $F_{ct,x}(t,w,w',\dot{w},\dot{w}')$ translated to the neutral axis of the plate, see Fig. 2.

2.1.2. Ice

As cavitation is not accounted for, continuity between ice and fluid dictates that their vertical displacements must be the same along their interface:

$$w(x,t) = \frac{\partial \phi(x,0,t)}{\partial z} \quad \forall \ x \in (\infty,0] \tag{5}$$

To complete the description of the ice, two boundary conditions are needed at $x = 0$. The contact pressure generated by the interaction between ice and structure acts on the edge of the plate. This pressure is integrated and translated to the neutral axis of the plate, resulting in a
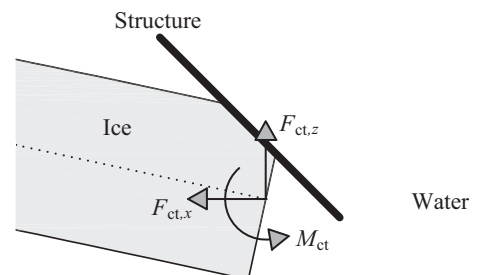

Fig. 1. The region $x \leq 0$ is referred to as the ice-covered region and the region $x > 0$ as the open water region.

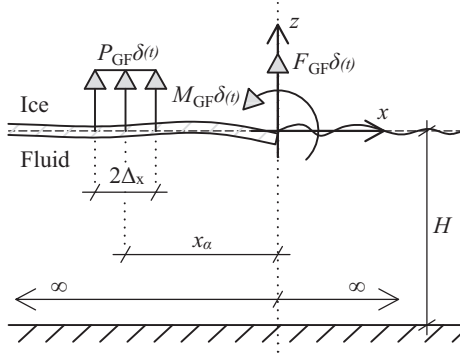**Fig. 2.** The decomposition of the contact force.

Fig. 3. The problem definition for $\widetilde{\phi}_\alpha(x,z,\omega)$.

horizontal force $F_{\mathrm{ct,x}}(t,w,w',\dot{w},\dot{w}')$, vertical force $F_{\mathrm{ct,z}}(t,w,w',\dot{w},\dot{w}')$ and moment $M_{\mathrm{ct}}(t,w,w',\dot{w},\dot{w}')$, see Fig. 2. These three loads are assumed to act on the edge of the plate and therefore enter its boundary conditions located at $x = 0$. These boundary conditions enforce a balance of forces and moments at the edge of the plate:

$$\frac{E}{1-\nu^2}\frac{h^3}{12}\frac{\partial^3 w(0,t)}{\partial x^3} + (F_{\mathrm{ct,x}}(t,w,w',\dot{w},\dot{w}')w')|_{x=0}$$
$$= (F_{\mathrm{ct,z}}(t,w,w',\dot{w},\dot{w}'))|_{x=0} \tag{6a}$$

$$\frac{E}{1-\nu^2}\frac{h^3}{12}\frac{\partial^2 w(0,t)}{\partial x^2} + (F_{\mathrm{ct,x}}(t,w,w',\dot{w},\dot{w}')w)|_{x=0}$$
$$= (M_{\mathrm{ct}}(t,w,w',\dot{w},\dot{w}'))|_{x=0} \tag{6b}$$

where the first term in both equations is due to the bending stiffness of the plate and the second term is due to axial compression. As the loads act on the edge of the plate, they are per unit meter. These contact loads are calculated with the contact model described in Keijdener and Metrikine (2014). This contact model is piece-wise linear as it switches between two linear modes of interaction. As the moment of transition between the two modes is not known in advance, the contact model is nonlinear in time. A qualitative description of the contact model is given in Section 4.3.

The ice continues to move down the structure until the ice fails in bending. Failure is defined as the moment in time t_{fail} when the axial stresses first exceed the ice's flexural strength σ_{fl}. Although axial deformations are not included in this model, the contribution of the axial force to the axial compression is included in the failure criterion:

$$\sigma_{\max}(x,t) = \left| \frac{Eh}{2(1-\nu^2)}w''(x,t) \right|$$
$$- \frac{F_{\mathrm{ct,x}}(t,w,w',\dot{w},\dot{w}')}{h} \le \sigma_{\mathrm{fl}} \tag{7}$$

where the max-subscript implies the maximum stress within the cross-section of the ice.

2.2. Solution method

The approach for solving the above-formulated dynamical problem is discussed next. The problem is nonlinear due to (i) the nonlinear dynamic pressure in Eq. (3), (ii) the state-dependent axial compression in the plate, Eq. (4), and (iii) the state-dependent contact loads, Eq. (6). The problem is solved using the framework of the pseudo-force approach (Aprile et al., 1994). In accordance with this approach, the solution procedure is based on the solution of the linear part of the problem, which in this work is expressed in terms of the Green's functions. The steps of the procedure are as follows. At each time step, the system is assumed to be linear and the nonlinear components of the model are accounted for by means of pseudo forces. Basically, the nonlinear terms are moved to the right-hand side of the equations of motion and the

resulting implicit equations are solved in an iterative manner. In order to deal with the distributed nonlinear loads (the dynamic pressure and the axial compression), these are assumed to be piece-wise constant in space. The steps of the procedure are presented in detail below.

2.2.1. Green's functions

Three frequency-domain Green's functions are computed first, neglecting all nonlinearities in the problem statement. These Green's functions, computed for the system and loads shown in Fig. 3, represent the response of the system to (i) the force $F_{\mathrm{GF}}\delta(t)$ applied at the edge of the plate, (ii) the moment $M_{\mathrm{GF}}\delta(t)$ applied at the edge of the plate, (iii) a uniformly distributed vertical force $P_{\mathrm{GF}}\delta(t)$ applied to a segment of the plate. The segment has a width of $2\Delta_{\mathrm{x}}$ and is centered around x_α:

$$x_\alpha = -2\Delta_{\mathrm{x}}(\alpha - 1/2) \tag{8}$$

where α identifies the location of the segment.

The frequency domain response of the system to all the three loads shown in Fig. 3 is captured in a single potential $\widetilde{\phi}_\alpha(x,z,\omega)$. As the approach used to derive this potential is explained in Keijdener et al. (2017), all derivations are omitted and only the final form is presented:

$$\widetilde{\phi}_\alpha(x,z,\omega) = \begin{cases} \widetilde{\phi}_\alpha^{(\mathrm{p})}(x,z,\omega) + \widetilde{\phi}_\alpha^{(-)}(x,z,\omega), \\ \quad \forall \quad x \in (-\infty,0] \cap z \in [-H,0] \\ \widetilde{\phi}_\alpha^{(+)}(x,z,\omega), \\ \quad \forall \quad x \in (0,\infty) \cap z \in [-H,0] \end{cases} \tag{9}$$

The waves excited by the distributed force $P_{\mathrm{GF}}\delta(t)$ are captured in $\widetilde{\phi}_\alpha^{(\mathrm{p})}$. These waves are transmitted and reflected by the inhomogeneity at $x = 0$, resulting in a second set of waves that propagate horizontally away from $x = 0$. In addition, a third set of waves are generated by the contact loads $F_{\mathrm{GF}}\delta(t)$ and $M_{\mathrm{GF}}\delta(t)$ that also propagate away from $x = 0$. The waves of the secondary and third set that propagate towards $-\infty$ are captured in $\widetilde{\phi}_\alpha^{(-)}$ while those propagating towards $+\infty$ are captured in $\widetilde{\phi}_\alpha^{(+)}$. As the response in the open-water region, $x \in (0,\infty)$, is not needed for the analyses performed in this paper, the expression of $\widetilde{\phi}_\alpha^{(+)}$ is not given.

The expressions for the two remaining potentials are given next, starting with $\widetilde{\phi}_\alpha^{(\mathrm{p})}(x,z,\omega)$:

$$\widetilde{\phi}_\alpha^{(\mathrm{p})}(x,z,\omega) = -\frac{P_{\mathrm{GF}}}{\rho_w g}\sum_{n=0}^{N_{\mathrm{k}}}\gamma_n Q_n^{-1}I_{\alpha,n}(x)Z_n(z) \tag{10}$$

The solution is a superposition of the modes of the ice-covered region. The shape of these modes is defined by the vertical wavenumbers k_n of the system. These wavenumbers are given by the roots of the dispersion relation of the ice-covered region $kD(k) = 0$:

$$D(k) = \delta k^4 + 1 - a(\gamma + \lambda^{-1}(k)) \tag{11}$$

where k is the wavenumber, $a = \omega^2/g$, ω is frequency, $\gamma = h\rho_i/\rho_w$ and $\delta = Eh^3/(12\rho_w g)/(1-\nu^2)$. The roots are collected in the set $k_n \mid n \in \mathbb{Z}_0$ which is defined as follows:

- $k_0 = 0$
- k_1: the complex root in the first quadrant.
- k_2: the complex root in the second quadrant.
- k_3: the negative real root.
- k_n, $n \ge 4$: the positive imaginary roots in ascending order.

The infinite summation in Eq. (10) was truncated at N_{k}. k_0 falls on the integration path and so had to be excluded. The Cauchy principal value of this root contributes only half as much as the other roots that are all located inside the contour. γ_n in Eq. (10) accounts this difference:

$$\gamma_n = \begin{cases} 1/2, & \text{if } n = 0 \\ 1, & \text{if } n > 0 \end{cases} \tag{12}$$

Continuing with the remaining terms in Eq. (10), Q_n is given by:

$$Q_n = D_n(2\lambda_n + H(k_n^2 - \lambda_n^2))$$
$$+ 4\delta k_n^4 \lambda_n + a\left(1 + \frac{H(k_n^2 - \lambda_n^2)}{\lambda_n}\right) \tag{13}$$

where $D_n = D(k_n)$ and $\lambda_n = \lambda(k_n) = Z'(k_n, 0) = k_n \tanh(k_n H)$. The depth eigenfunction $Z(k, z)$ is given by:

$$Z(k, z) = \frac{\cosh(k(z + H))}{\cosh(kH)} \tag{14}$$

The x-dependency of $\widetilde{\phi}_\alpha$ is captured in $I_{\alpha, n}(x)$:

$$I_{\alpha,n}(x) = \text{sgn}(x - x_\alpha^+) e^{ik_n|x - x_\alpha^+|}$$
$$- \text{sgn}(x - x_\alpha^-) e^{ik_n|x - x_\alpha^-|} \tag{15}$$

where $x_\alpha^+ = x_\alpha + \Delta_x$, $x_\alpha^- = x_\alpha - \Delta_x$, $i = \sqrt{-1}$ and the derivatives of $I_{\alpha, n}(x)$ are given by:

$$\frac{\partial^q I_{\alpha,n}(x)}{\partial x^q} = (ik_n)^q \left(\text{sgn}(x - x_\alpha^+)^{q-1} e^{ik_n|x - x_\alpha^+|} \right.$$
$$\left. - \text{sgn}(x - x_\alpha^-)^{q-1} e^{ik_n|x - x_\alpha^-|} \right) \tag{16}$$

Continuing with the second potential, $\widetilde{\phi}_\alpha^{(\cdot)}(x, z, \omega)$ is given by:

$$\widetilde{\phi}_\alpha^{(\cdot)}(x, z, \omega) = \sum_{n=1}^{N_k} a_{\alpha,n} e^{-ik_n x} Z_n(z) \tag{17}$$

The amplitudes $a_{\alpha, n}$ are obtained by solving a set of N_k equations defined below. The set was established through the eigenfunction matching procedure. The first two equations assure that the linearized version of the boundary conditions for the plate in Eq. (6) are satisfied. The set of the remaining $N_k - 2$ equations assure that the fluid's pressure and displacements are continuous at $x = 0$:

$$EI\left(\frac{P_{GF}}{\rho_w g} \sum_{n=1}^{N_k} \gamma_n Q_n^{-1} k_n^2 I''_{\alpha,n}(0)\lambda_n - \sum_{n=1}^{N_k} a_{\alpha,n} k_n^2 \lambda_n\right) = M_{GF} \tag{18a}$$

$$iEI\left(\frac{P_{GF}}{\rho_w g} \sum_{n=1}^{N_k} \gamma_n Q_n^{-1} k_n^3 I''_{\alpha,n}(0)\lambda_n + \sum_{n=1}^{N_k} a_{\alpha,n} k_n^3 \lambda_n\right) = F_{GF} \tag{18b}$$

$$\sum_{n=1}^{N_k} a_{\alpha,n} \frac{\lambda_n - \overline{\lambda}_j}{k_n - \overline{k}_j} = -\frac{P_{GF}}{\rho_w g} \sum_{n=1}^{N_k} Q_n^{-1}(k_n I'_{\alpha,n}(0) - \overline{k}_j I_{\alpha,n}(0)) \frac{\lambda_n - \overline{\lambda}_j}{k_n^2 - \overline{k}_j^2}$$
$$\forall \ j = 1 \cdot\cdot N_k - 2 \tag{18c}$$

where the summation starts at $n = 1$ because k_0 does not contribute to the response at $x = 0$, $\overline{\lambda}_j = \overline{k}_j \tanh(\overline{k}_j H)$ and $\overline{k}_j$ is the set of roots of the dispersion relation of the open water region:

$$a - \lambda(k) = 0 \tag{19}$$

which is defined as:

- $\overline{k}_1$: the negative real pole.
- $\overline{k}_j, j \geq 2$: the positive imaginary roots in ascending order.
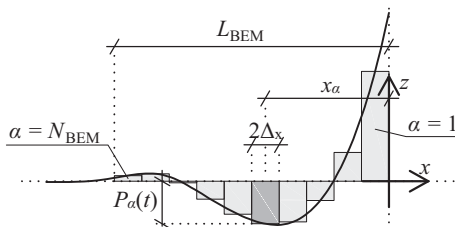

Fig. 4. The distributed nonlinear loads, depicted with the solid curve, are approximated using a piece-wise constant function. Note that $\forall \ x > 0$ the dynamic pressure is not accounted for.
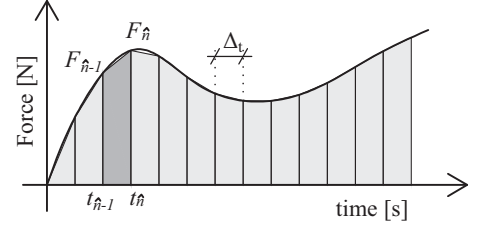

Fig. 5. All loads are approximated as piece-wise linear functions of time. The $\widehat{n}^{\text{th}}$ time step is highlighted.

2.2.2. Discretization of the distributed nonlinear forces

Two distributed nonlinear forces act on the ice, see Eq. (4), namely the axial compression and the dynamic pressure (the second term on the right-hand side of Eq. (3)). The axial compression is present $\forall \ x \in (-\infty, 0]$ while the dynamic pressure is present $\forall \ x \in (-\infty, \infty)$. It is assumed that the dynamic pressure can be ignored in the open water region and, consequently, the distributed nonlinear forces are only present in $x \in (-\infty, 0]$. This assumption is validated in Section 5.2. These loads are discretized as sketched in Fig. 4. The magnitude of these loads decreases with the distance from the contact point ($x = 0$). Therefore, only a finite length segment of the ice adjacent to the contact is discretized.

The truncation is done at $L_{BEM} = c_1 x_{bl}$, where x_{bl} is the static breaking length of the plate that corresponds to the used contact model (derived in AppendixA):

$$x_{bl} = \sqrt{2} \, l \text{atan}\left(\frac{\sqrt{2} l}{\sqrt{2} l - h \tan(\alpha)}\right) \tag{20}$$

where $l = \sqrt[4]{\delta}$, see Eq. (11). The resulting line segment of length L_{BEM} is discretized into N_{BEM} elements, each with a width of $2\Delta_x = L_{BEM}/N_{BEM}$, see Fig. 4. Within each element a constant, time-dependent distributed force $P_\alpha(t)$ applies. The elements are indexed with $\alpha = 1$. N_{BEM} are centered around x_α, see Eq. (8). This discretization assures that each element α corresponds with the surface pressure excitation of the Green's function $\widetilde{\phi}_\alpha$. How each element's $P_\alpha(t)$ is calculated is explained after the time-integration scheme has been introduced.

2.2.3. Time-integration

In order to perform the time-integration numerically, time is discretized using a constant time step Δ_t. Within each time step, the loads acting on the system, i.e. the pseudo-forces, are assumed to vary linearly with time. All the nonlinear loads are thus approximated as piece-wise linear functions of time, see Fig. 5. A state-dependent load $F(t, q(t))$ that depends on the state $q(t)$ (displacement, velocity, etc.) is thus approximated as:

$$F(t, q(t)) \approx \sum_{\widehat{n}=1}^{N_{time}} \widehat{F}_{\widehat{n}}(t, q_{\widehat{n}})$$
$$= \sum_{\widehat{n}=1}^{N_{time}} (\mathcal{H}(t - t_{\widehat{n}-1}) - \mathcal{H}(t - t_{\widehat{n}})) \times$$
$$\left(\frac{F_{\widehat{n}}(q_{\widehat{n}}) - F_{\widehat{n}-1}(q_{\widehat{n}-1})}{\Delta_t}(t - t_{\widehat{n}-1}) + F_{\widehat{n}-1}(q_{\widehat{n}-1})\right) \tag{21}$$

where $\mathcal{H}(t)$ is the Heaviside function, $N_{time} = T_{sim}/\Delta_t$ is the total number of time steps with T_{sim} being the simulation time, $t_{\widehat{n}} = \Delta_t \widehat{n}$ and all $\widehat{n}$-subscripts indicate evaluations at $t_{\widehat{n}}$.

The loading applied within time step $\widehat{n}$, $\widehat{F}_{\widehat{n}}(t, q_{\widehat{n}})$, is now decomposed into two parts, one proportional to $F_{\widehat{n}-1}(q_{\widehat{n}-1})$ and one proportional to $F_{\widehat{n}}(q_{\widehat{n}})$, see Fig. 6:

$$\widehat{F}_{\widehat{n}}(t, q_{\widehat{n}}) = F_{\widehat{n}-1}(q_{\widehat{n}-1})\widehat{\mathcal{L}}_{\widehat{n}}(t) + F_{\widehat{n}}(q_{\widehat{n}})\widehat{\mathcal{R}}_{\widehat{n}}(t) \tag{22}$$

where $\widehat{\mathcal{L}}_{\widehat{n}}(t)$ and $\widehat{\mathcal{R}}_{\widehat{n}}(t)$ are given by:

$$\widehat{\mathcal{L}}_{\hat{n}}(t) = (\mathcal{H}(t - t_{\hat{n}-1}) - \mathcal{H}(t - t_{\hat{n}}))$$
$$\times F_{\hat{n}-1}\left(1 - \frac{t - t_{\hat{n}-1}}{\Delta_t}\right) \tag{23a}$$

$$\widehat{\mathcal{R}}_{\hat{n}}(t) = (\mathcal{H}(t - t_{\hat{n}-1}) - \mathcal{H}(t - t_{\hat{n}}))$$
$$\times F_{\hat{n}} \frac{t - t_{\hat{n}-1}}{\Delta_t} \tag{23b}$$

The state $q(t)$ at $t = t_{\hat{n}}$ due to the loading applied within a single time step $\widehat{F}_{\hat{n}}(t, q_{\hat{n}})$ is thus computed as:

$$q_{\hat{n}} = F_{\hat{n}-1}(q_{\hat{n}-1})\mathcal{L}_{\hat{n}}\,|_{\hat{n}=0} + F_{\hat{n}}(q_{\hat{n}})\mathcal{R}_{\hat{n}}|_{\hat{n}=0} \tag{24}$$

where $\mathcal{L}_{\hat{n}}$ and $\mathcal{R}_{\hat{n}}$ are given by:

$$\mathcal{L}_n = \frac{1}{2\pi}\int_{-\infty}^{\infty} \widetilde{\mathcal{G}}(\omega)\widetilde{\mathcal{L}}(\omega)e^{i\omega\Delta_t n}d\omega \tag{25a}$$

$$\mathcal{R}_n = \frac{1}{2\pi}\int_{-\infty}^{\infty} \widetilde{\mathcal{G}}(\omega)\widetilde{\mathcal{R}}(\omega)e^{i\omega\Delta_t n}d\omega \tag{25b}$$

where $\widetilde{\mathcal{G}}(\omega)$ is the frequency domain Green's function corresponding to the state $q(t)$ and the load $F(t, q(t))$, and $\widetilde{\mathcal{L}}_{\hat{n}}(\omega)$ and $\widetilde{\mathcal{R}}_{\hat{n}}(\omega)$ are given by:

$$\widetilde{\mathcal{L}}(\omega) = \frac{1}{\omega^2\Delta_t}(e^{i\omega\Delta_t}(1 - i\omega\Delta_t) - 1) \tag{26a}$$

$$\widetilde{\mathcal{R}}(\omega) = \frac{1}{\omega^2\Delta_t}(1 + i\omega\Delta_t - e^{i\omega\Delta_t}) \tag{26b}$$

The inverse Fourier transforms in Eqs. (25) are evaluated numerically using a quadratic, nested, adaptive integration scheme. The scheme observes a global error criterion that assures the time-domain error of $\mathcal{L}_n$ and $\mathcal{R}_n$ is below a specified relative and absolute tolerance for all $t \in [0, T_{\text{sim}}]$.

Eq. (24) only accounts for the response to the loading that was applied during the current time step. The state q_n which is the response to the load $F(t, q(t))$ at $t = t_n = \Delta_t n$ is obtained as:

$$q_n \approx \sum_{\hat{n}=1}^{n} F_{\hat{n}-1}(q_{\hat{n}-1})\mathcal{L}_{n-\hat{n}} + F_{\hat{n}}(q_{\hat{n}})\mathcal{R}_{n-\hat{n}} \tag{27}$$

This implicit equation is solved at each time step. The iterative scheme used will be explained next, but first Eq. (27) is generalized. Eq. (27) only accounts for a single pseudo-force, and thus only a single nonlinear load, while the scheme has to account for multiple nonlinear loads. Likewise, only a single state-component $q(t)$ was considered while multiple are needed. Now, let $\mathbf{q}(t)$ be the state-vector of length N_q that contains all the required state-components, the value of each state-component is then obtained by superimposing the contributions of all pseudo-forces:

$$\mathbf{q}_n \approx \sum_{\hat{n}=1}^{n}\left(\sum_{\alpha=1}^{N_F} F_{\hat{n}-1}^{(\alpha)}(\mathbf{q}_{\hat{n}-1})\mathcal{L}_{n-\hat{n}}^{(\alpha)} + F_{\hat{n}}^{(\alpha)}(\mathbf{q}_{\hat{n}})\mathcal{R}_{n-\hat{n}}^{(\alpha)}\right) \tag{28}$$

where α is the identifier of the nonlinear loads, N_F is the total number of nonlinear loads, $\mathcal{L}_n^{(\alpha)}$ and $\mathcal{R}_n^{(\alpha)}$ are based on Eqs. (25) but now using the set of N_q Green's functions $\widetilde{\mathcal{G}}_\alpha(\omega)$ that contain the frequency-domain response of each state-component in $\mathbf{q}_n$ excited by the load specified by
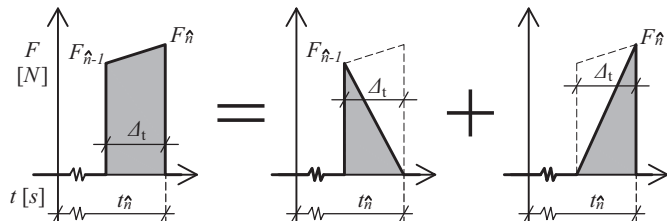

Fig. 6. The loading applied within a single time-step $\widehat{F}_{\hat{n}}(t, q_{\hat{n}})$ is decomposed into two parts: one proportional to $F_{\hat{n}-1}$ and the other proportional to $F_{\hat{n}}$.

the index α.

In order to advance to the next time step, Eq. (28) is solved for $\mathbf{q}_n$. In agreement with the pseudo-force approach this is done using an iterative scheme. The scheme is defined by the following recursive relation that starts at $i = 0$:

$$\mathbf{q}_n^{[i+1]} \approx \mathbf{q}_n^{[0]} + \sum_{\alpha=1}^{N_F} F_n^{(\alpha)}(\mathbf{q}_n^{[i]})\mathcal{R}_0^{(\alpha)} \tag{29}$$

where the state-vector $\mathbf{q}_n^{[0]}$ contains the response at t_n due to the loading at all previous time steps:

$$\mathbf{q}_n^{[0]} = \sum_{\hat{n}=1}^{n-1}\sum_{\alpha=1}^{N_F} (F_{\hat{n}-1}^{(\alpha)}(\mathbf{q}_{\hat{n}-1})\mathcal{L}_{n-\hat{n}}^{(\alpha)} + F_{\hat{n}}^{(\alpha)}(\mathbf{q}_{\hat{n}})\mathcal{R}_{n-\hat{n}}^{(\alpha)})$$
$$+ \sum_{\alpha=1}^{N_F} F_{n-1}^{(\alpha)}(\mathbf{q}_{n-1})\mathcal{L}_0^{(\alpha)} \tag{30}$$

The rate of convergence of this iterative scheme is $\mathcal{R}_0^{(\alpha)}$. Iterations continues until the specified tolerances are met for all entries of the state-vector $\mathbf{q}_n$. The scheme converges in two to five iterations depending on the tolerances used. No convergence problems were encountered while computing the results for this paper.

2.2.4. Applying the time-integration scheme

The time-integration scheme is now used to calculate the time-domain response of the dynamical problem defined in Subsection 2.1.

For this problem the set of pseudo-forces $F^{(\alpha)}(t, \mathbf{q}(t))$ contains a total of $N_F = N_{\text{BEM}} + 2$ forces:

$$F^{(\alpha)}(t) = P_\alpha(t) = -\frac{\rho_w}{2}\left(\left(\frac{\partial\dot{\phi}^{(\alpha)}}{\partial x}\right)^2 + \left(\frac{\partial\dot{\phi}^{(\alpha)}}{\partial z}\right)^2\right)$$
$$+ F_{\text{ct,x}}(t, w, w', \dot{w}, \dot{w}')\frac{\partial^2 w^{(\alpha)}}{\partial x^2}$$
$$\forall \quad \alpha = 1\cdot\cdot N_{\text{BEM}} \tag{31a}$$

$$F^{(N_{\text{BEM}}+1)}(t) = F_{\text{ct,z}}(t, w, w', \dot{w}, \dot{w}')$$
$$- (F_{\text{ct,x}}(t, w, w', \dot{w}, \dot{w}')w')|_{x=0} \tag{31b}$$

$$F^{(N_{\text{BEM}}+2)}(t) = M_{\text{ct}}(t, w, w', \dot{w}, \dot{w}')|_{x=0}$$
$$- (F_{\text{ct,x}}(t, w, w', \dot{w}, \dot{w}')w)|_{x=0} \tag{31c}$$

where the superposition of the first N_{BEM} pseudo-forces results in the piece-wise approximation of the nonlinear distributed forces, see Fig. 4, and the last two pseudo-forces account for the state-dependent loading at the contact, see Eq. (6). Because the distributed forces vary within each element, a representative force must be used. This is chosen to be equal to the mean value of the force within the element.

The state-dependent loads $F^{(\alpha)}(t, \mathbf{q}(t))$ depend on several state-component. These are collected in the state-vector $\mathbf{q}(t)$ of length $N_q = 4 + 3N_{\text{BEM}}$:

$$\mathbf{q}(t) = \left[w, w', \dot{w}, \dot{w}', \frac{\partial\dot{\phi}^{(1)}}{\partial x}\cdot\cdot\frac{\partial\dot{\phi}^{(N_{\text{BEM}})}}{\partial x},\right.$$
$$\left.\frac{\partial\dot{\phi}^{(1)}}{\partial z}\cdot\cdot\frac{\partial\dot{\phi}^{(N_{\text{BEM}})}}{\partial z}, \frac{\partial^2 w^{(1)}}{\partial x^2}\cdot\cdot\frac{\partial^2 w^{(N_{\text{BEM}})}}{\partial x^2}\right]^T \tag{32}$$

where w, w', $\dot{w}$, and $\dot{w}'$ are used to evaluate the pseudo-forces related to the contact loads, Eqs. (31b) and (31c), and $\frac{\partial\dot{\phi}^{(\beta)}}{\partial x}$, $\frac{\partial\dot{\phi}^{(\beta)}}{\partial z}$ and $\frac{\partial^2 w^{(\beta)}}{\partial x^2}$ are needed to evaluate the N_{BEM} pseudo-forces related to the discretized nonlinear distributed forces, Eq. (31a).

All derivatives in $\mathbf{q}(t)$ are computed using finite differences of the corresponding displacements. This is done because the inverse Fourier transform of the displacements converge significantly faster than those of the derivatives. In particular, for the velocities a backward scheme is used. The order of the scheme starts at one and increases up to four as t_n

increases. For the slope w' a first order backward scheme is used and for the curvature w'' a second order central difference scheme. Using finite differences to compute the derivatives increases the errors present in the displacements. Therefore, $\mathcal{L}_n^{(\alpha)}$ and $\mathcal{R}_n^{(\alpha)}$ need to be computed using strict tolerances and Δ_t and Δ_x need to be sufficiently small. Since all derivatives are computed using finite differences, these state-components no longer have to be computed using the convolution that is embedded in Eq. (29). Consequently, the following reduced state-vector of length $\widehat{N}_\beta$ is introduced that excludes these state-components:

$$\widehat{\mathbf{q}}(t) = \left[w, \frac{\partial \phi^{(1)}}{\partial x} \cdot \cdot \frac{\partial \phi^{(N_{\mathrm{BEM}})}}{\partial x}, \frac{\partial \phi^{(1)}}{\partial z} \cdot \cdot \frac{\partial \phi^{(N_{\mathrm{BEM}})}}{\partial z} \right]^T \tag{33}$$

The full state-vector $\mathbf{q}_n$ can then be computed from $\widehat{\mathbf{q}}_n$ using the relevant finite difference relations. Eq. (29) is updated accordingly:

Starting at $i = 0$

1. $\quad \mathbf{q}_n^{[i]} \approx \mathcal{D}\left(\widehat{\mathbf{q}}_n^{[i]}, \widehat{\mathbf{q}}_{n-1}^{[i]} \cdot \cdot \widehat{\mathbf{q}}_{n-d}^{[i]} \right) \tag{34a}$

2. $\quad \widehat{\mathbf{q}}_n^{[i+1]} \approx \widehat{\mathbf{q}}_n^{[0]} + \sum_{\alpha=1}^{N_F} F_n^{(\alpha)}(\mathbf{q}_n^{[i]}) \mathcal{R}_0^{(\alpha)} \tag{34b}$

where the finite difference operator $\mathcal{D}$ computes $\mathbf{q}_n^{[i]}$ based on the current as well as the last d reduced state-vectors. d starts at 0 for $n = 1$ and increases up to 4 in order to have enough data points to evaluate the fourth order finite difference scheme used for computing the velocities.

For each state-component $q(t)$ the contribution of all pseudo-forces must be superimposed. This means that a total of $\widehat{N}_\beta \times N_F$ frequency-domain Green's functions are needed to relate all pseudo-forces in $F^{(\alpha)}(t, \mathbf{q}(t))$ with all state-components in $\widehat{\mathbf{q}}(t)$. These Green's functions are based on $\widetilde{\phi}_\alpha$, given by Eq. (9):

$$\widetilde{G}_\alpha(\omega) = \left[\widetilde{\phi}_\alpha(0,0,\omega), \frac{\partial \widetilde{\phi}_\alpha^{(1)}(0,\omega)}{\partial x} \cdot \cdot \frac{\partial \widetilde{\phi}_\alpha^{(N_{\mathrm{BEM}})}(0,\omega)}{\partial x}, \right.$$
$$\left. \frac{\partial^0 \widetilde{\phi}_\alpha^{(1)}(0,\omega)}{\partial z^0} \cdot \cdot \frac{\partial \widetilde{\phi}_\alpha^{(N_{\mathrm{BEM}})}(0,\omega)}{\partial z} \right]^T$$
$$\forall \quad \alpha = 1 \cdot \cdot N_F \tag{35}$$

$\widetilde{\phi}_\alpha(x,z,\omega)$ is a superposition of the response to three generalized force: P_{GF}, F_{GF} and M_{GF}. For each specific value of α only one of these three forces is activated, according to the following definition:

for $\alpha = 1 \cdot \cdot N_{\mathrm{BEM}}$, $\quad P_{\mathrm{GF}} = 1, F_{\mathrm{GF}} = 0, M_{\mathrm{GF}} = 0$
for $\alpha = N_{\mathrm{BEM}} + 1$, $\quad P_{\mathrm{GF}} = 0, F_{\mathrm{GF}} = 1, M_{\mathrm{GF}} = 0$
for $\alpha = N_{\mathrm{BEM}} + 2$, $\quad P_{\mathrm{GF}} = 0, F_{\mathrm{GF}} = 0, M_{\mathrm{GF}} = 1 \tag{36}$

and the Green's function of the mean horizontal displacement of the fluid within element $\beta = -\infty \cdot \cdot 0$ is computed using:

$$\frac{\partial \widetilde{\phi}_\alpha^{(\beta)}(0,\omega)}{\partial x} = \frac{1}{2\Delta_x} \int_{x_\beta^-}^{x_\beta^+} \frac{\partial \widetilde{\phi}_\alpha(x,0,\omega)}{\partial x} dx$$
$$- \frac{P_{\mathrm{GF}}}{\rho_w g} \frac{1}{2\Delta_x} \sum_{n=0}^{N} \gamma_n Q_n^{-1} I'_{\alpha,\beta,n} Z_n(0)$$
$$- \frac{i}{\Delta_x} \sum_{n=1}^{N} a_{\alpha,n} \sin(k_n \Delta_x) e^{-ik_n x_\beta} Z_n(0) \tag{37}$$

where $I'_{\alpha,\beta,n}$ is given by:

$$I'_{\alpha,\beta,n} = \int_{x_\beta^-}^{x_\beta^+} \frac{\partial I'_{\alpha,n}(x)}{\partial x} dx$$
$$= \begin{cases} 2\,\mathrm{sgn}(\beta - \alpha)(1 - \cos(2k_n \Delta_x)) e^{ik_n |x_\beta - x_\alpha|}, & \text{if } \beta \neq \alpha \\ 0, & \text{if } \beta = \alpha \end{cases} \tag{38}$$

The Green's function of the mean vertical displacement of both the ice and the fluid within element β is computed using:

$$\frac{\partial \widetilde{\phi}_\alpha^{(\beta)}(0,\omega)}{\partial z} = \frac{1}{2\Delta_x} \int_{x_\beta - \Delta_x}^{x_\beta + \Delta_x} \frac{\partial \widetilde{\phi}_\alpha(0,\omega)}{\partial z} dx$$
$$- \frac{P_{\mathrm{GF}}}{\rho_w g} \frac{1}{2\Delta_x} \sum_{n=0}^{N} \gamma_n Q_n^{-1} I_{\alpha,\beta,n} Z_n'(0)$$
$$+ \frac{1}{\Delta_x} \sum_{n=1}^{N} a_{\alpha,n} \frac{\sin(k_n \Delta_x)}{k_n \Delta_x} e^{-ik_n x_\beta} Z_n'(0) \tag{39}$$

where $I_{\alpha,\beta,n}$ is given by:

$$I_{\alpha,\beta,n} = \int_{x_\beta - \Delta_x}^{x_\beta + \Delta_x} I_{\alpha,n}(x) dx$$
$$= \frac{-4}{k_n \Delta_x} \begin{cases} \sin(\Delta_x k_n) e^{i \Delta_x k_n}, & \text{if } \alpha = \beta \\ i\sin^2(\Delta_x k_n) e^{2i \Delta_x k_n |\alpha - \beta|}, & \text{if } \alpha \neq \beta \end{cases} \tag{40}$$

Employing the above-described procedure, the breaking length of the ice sheet, which is the key output the paper focuses upon, is computed using a cubic spline interpolation of the axial stress of each element.

3. Validation

The proposed model is validated in this section. The time-integration is addressed first, followed by a validation of the proposed ice-structure interaction model.

3.1. Validation of the time-integration scheme

In order to validate the time-integration scheme, the analytical time-domain solution of a floating ice plate obtained by Zhao and Dempsey (1996) is chosen as a benchmark. They considered, in a 2D context, the response of an infinite ice plate floating on a finite depth fluid layer to the load $F(t) = \delta(x)\mathcal{H}(t)$. The ice is modeled as a Kirchhoff-Love plate, the fluid is described by the Laplace equation and its pressure on the ice by the linearized Bernoulli equation.

The approach presented in the current paper was applied to the same model. The following set of parameters was used for this validation case: $h = 1$ m, $\rho_i = 925$ kg/m³, $\rho_w = 1025$ kg/m³, $g = 9.81$ m/s², $H = 4l$ m where $l = 4\sqrt[4]{\delta}$ see Eq. (4), $E = (10h)^4 \rho_w g/(h^3/12)$ Pa, $\nu = 0.3$, $N_{\mathrm{BEM}} = 40$, $2\Delta_x = 4\,l/N_{\mathrm{BEM}}$, $\Delta_t = 1 \times 10^{-3}$ s and $N_k = 500$. The value of all numerical parameters are based on extensive convergence studies.

Application of the procedure introduced in this paper results in a single state-independent pseudo-force: $F^{(1)}(t) = \mathcal{H}(t)$. The state-vector $\mathbf{q}(t)$ contains the response of the plate as a function of x shown in Fig. 7. The corresponding set of Green's functions are approximated by taking $\widetilde{\phi}_\alpha^{(p)}$, given by Eq. (10), letting Δ_x approach zero and evaluating this function at the relevant values of $\bar{x} = x/l \mid l = \sqrt[4]{\delta}$, see Eq. (11):
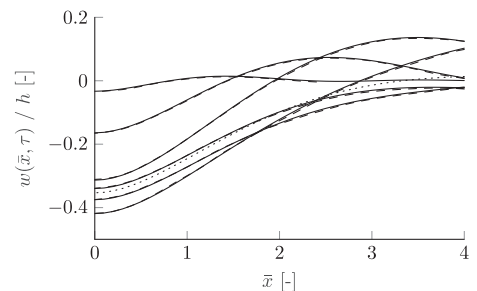
Fig. 7. The normalized, transient, vertical response of the ice. The solid lines show the response of the proposed model and the dashed lines are the results from Zhao and Dempsey (1996). The lines, from top to bottom, are evaluations at $\tau = t\sqrt{g/l} = \{0.25, 1, 2, 8, 6, 4\}$ respectively. The dotted line shows the static response.

$$\widetilde{\mathscr{G}}(\overline{x}, \omega) = \lim_{\Delta_x \to 0} \tilde{\phi}_{1/2}^{(p)}(\overline{x}, 0, \omega) \tag{41}$$

where the evaluation at $\alpha = 1/2$ assures that the load is applied at $x = 0$.

Fig. 2.a of Zhao and Dempsey (1996) has been reproduced in Fig. 7. This figure shows the time-domain response of the plate at several locations and moments in time. The figure shows that the results of both approaches agree very well.

3.2. Validation of the ISI model

In order to validate the proposed ISI model, its predictions are compared with the experimental work done by Valanto (1992). In Valanto's experimental campaign the 2D interaction between level ice and a downward sloping plate was studied for a range of ice velocities. The measurements of interest are the maximum horizontal contact force and the breaking length, both as functions of the ice velocity.

In correspondence with the experiments, see also (Wang and Poh, 2017), the following parameters were used in the numerical procedure: $h = 1/33.33$ m, $\rho_i = 916$ kg/m^3, $\rho_w = 1025$ kg/m^3, $g = 9.81$ m/s^2, $H = 1$ m, $E = 140 \times 10^6$ Pa, $\nu = 0.3$, $\sigma_c = 11 \times 10^3$ Pa, $\sigma_{fl} = 25 \times 10^3$ Pa, ice-steel friction coefficient $\xi = 0.1$ [−], width $b = 0.340$ m, $\theta = 15°$. $N_{BEM} = 60$, $c_1 = 1.25$, $\Delta_t = 5 \times 10^{-4}$ s and $N_k = 250$.

In the experimental setup of Valanto the geometry of the icebreaker is accounted for while in the proposed model it is not. To mimic the structure's presence, a semi-infinite problem is considered, see Fig. 8. This approach was also adopted by other authors who used this case for validation (Valanto, 1992; Wang and Poh, 2017).

All equations presented in Section 2 remain valid with one exception. The set of $N_k - 2$ equations Eq. (18c) that assures the continuity of the fluid's displacement and pressure at $x = 0$ has to be replaced by the following set of equations:

$$\sum_{n=1}^{N_k} -a_{\alpha,n} k_n \frac{\lambda_n - \overline{\lambda}_j}{k_n - \overline{k}_j} = \frac{P_{GF}}{\rho_w g} \sum_{n=1}^{N_k} Q_n^{-1} k_n I'_{\alpha,n}(0) \frac{\lambda_n - \overline{\lambda}_j}{k_n^2 - \overline{k}_j^2}$$
$$\forall \ j = 1 \cdot \cdot N_k - 2 \tag{42}$$

This set assures that the horizontal displacement of the fluid is zero at $x = 0$.

3.2.1. Breaking length

In Fig. 9 the breaking lengths predicted by the semi-infinite version of the proposed model are compared with those measured during the experiments done by Valanto (1992).

At high velocities, the proposed model predicts slightly smaller breaking lengths. A possible explanation for this discrepancy could be that during the experiments the ice slab, which was 334 to 340 mm wide, had two slits running alongside it, each with a width of 5–8 mm. As fluid can flow into these slits, their presence alleviates the build-up of fluid pressure under the ice. This phenomenon is discussed in Valanto (1992). Reducing the hydrodynamic pressure means that the ice
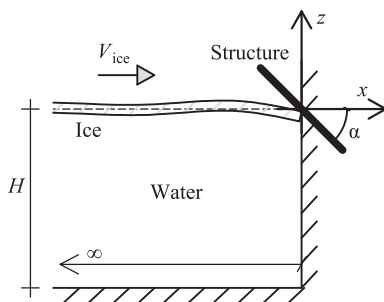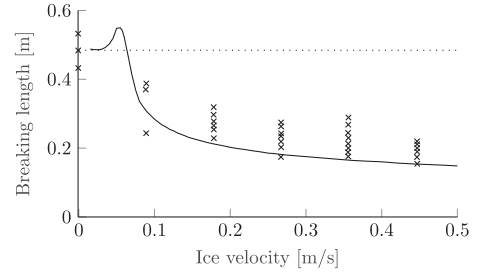

Fig. 9. The breaking length as a function of the ice velocity. The crosses represent the experimental data. The curve shows the values predicted by the proposed model. The dotted line is the static breaking length.

experiences less resistance as it deflects downwards, thereby reducing the bending stresses generated. This, in turn, causes the ice to fail later during the interaction process, thereby increasing the breaking length.

At low velocities, the proposed model predicts a velocity range wherein the ice fails statically. No experiments were done in this range and so this phenomenon cannot be validated. The transition from quasi-static to dynamic failure is studied in detail in the next section.

3.2.2. Maximum horizontal contact force

The maximum horizontal contact force (MHCF) is compared in Fig. 10. The MHCF predicted by the proposed model agrees well with the measured one at lower velocities but as the ice velocity increases, the model increasingly underpredicts the MHCF. A possible explanation for this could be that the horizontal component of the fluid pressure due to the stationary flow around the hull is not accounted for in the proposed model.

4. Results

In this section, the results of the numerical analysis of the model are presented. The focus is first placed on assessing the relative importance of the forces that act on the ice. Thereafter, the interdependence of the temporal development of the contact force and the dependence of the breaking length on the ice velocity is studied. Finally, the limitations of the hydrostatic model are addressed.

The results presented in this section have been computed using the following set of full-scale parameters (Timco and Weeks, 2010): $h = 1$ m, $\rho_i = 925$ kg/m^3, $\rho_w = 1025$ kg/m^3, $g = 9.81$ m/s^2, $H = 100$ m, $E = 5 \times 10^9$ Pa, $\nu = 0.3$, $\sigma_c = 6 \times 10^5$ Pa, $\sigma_{fl} = 5 \times 10^5$ Pa, ice-steel friction coefficient $\xi = 0.1$ [−] and hull angle $\theta = 45°$. The value of all numerical parameters are based on extensive convergence studies and are given as: $N_{BEM} = 60$, $c_1 = 1.25$, $\Delta_t = 10^{-3}$ s, $N_{modes} = 250$.

4.1. Determining the factors of influence for ISI

In this model there are in total seven forces that affect the dynamic equilibrium of the ice. The terms representing these forces together
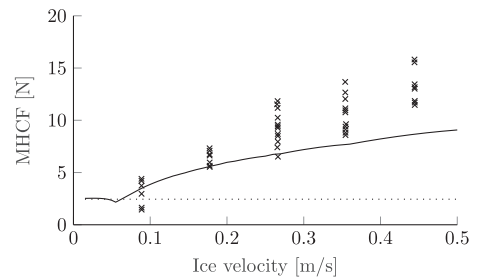

Fig. 8. For validation a semi-infinite model is considered.

Fig. 10. The MHCF for a range of ice velocities. The crosses show the experimental data. The values predicted by the proposed model are shown by the curve. The dotted line is the static MHCF.
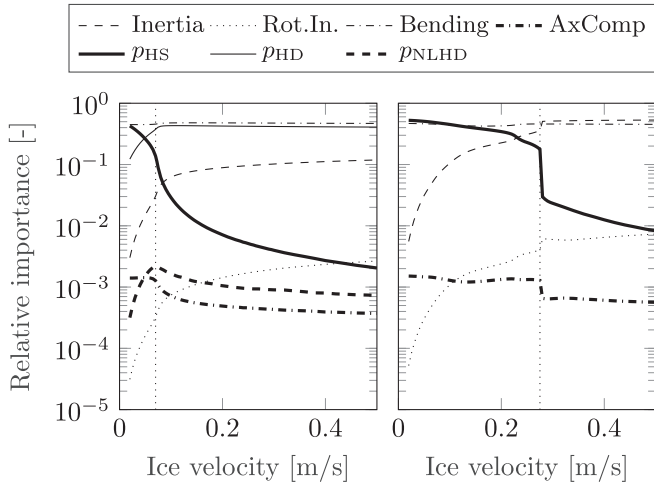
Fig. 11. The relative importance R_j of all seven terms. Left: hydrodynamic model. Right: hydrostatic model. The vertical dotted lines indicate the transition velocity $V_{s \to d}$ that separates the quasi-static and dynamic interactions. $V_{s \to d}$ is discussed in detail in Subsection 4.3.

form the equation of motion of the ice, Eq. (4), and are related to: the inertia of the ice, the rotational inertia of the ice, bending, axial compression, hydrostatic pressure p_{HS}, linear hydrodynamic pressure p_{HD} and nonlinear hydrodynamic pressure p_{NLHD}.

In order to determine the relative importance of the above-mentioned forces, the contribution of each of the seven terms to the balance of forces is studied. This is done by using the following measure:

$$R_j = \frac{\int_0^{t_{fail}} \int_{-L_{BEM}}^0 \left| p_j(x, 0, t) \right| \mathrm{d}x \mathrm{d}t}{\sum_{i=1}^7 \int_0^{t_{fail}} \int_{-L_{BEM}}^0 \left| p_i(x, 0, t) \right| \mathrm{d}x \mathrm{d}t}$$

(43)

where i and j imply indexing over the seven terms listed before. The absolute magnitude of each term is averaged in both space, for $x \in [-L_{BEM}, 0]$, and in time, starting from $t = 0$ until the ice fails in bending at $t = t_{fail}$. This average contribution is then normalized, thereby characterizing the significance of each term relative to all the other terms. The left graph in Fig. 11 shows the relative importance R_j of each of the seven terms.

The pressure that the fluid exerts on the ice is described by three terms forming the right-hand side of Eq. (3). The hydrodynamic component of this pressure is given by two of these terms: $p_{HD} = -\rho_w \ddot{\phi}$ and $p_{NLHD} = -\rho_w \frac{1}{2} v^2$. To the authors' knowledge, the relative importance of these two terms has not been documented in literature. The left graph in Fig. 11 shows that the relative importance of p_{NLHD} is about thousand times smaller than the relative importance of p_{HD}. All of the hydrodynamic effects can thus be attributed to p_{HD}. From this, it can be concluded that p_{NLHD} is not a factor of influence for ISI. Since p_{NLHD} incurs a significant calculation cost in the proposed model, it is ignored in the remainder of this paper.

Of the four terms related to the internal ice forces, two have a marginal contribution, namely; the rotational inertia of the ice and the axial compression. These two terms are also ignored in the remainder of this paper.

Based on these findings it can be concluded that of the seven terms studied, only four terms are important for ISI. Listed in the order of importance, the factors of influence for ISI are thus: bending of the ice, the linear hydrodynamic pressure p_{HD}, the hydrostatic pressure p_{HS} and the inertia of the ice.

4.2. Balance of forces in the ice

Four factors of significant influence were identified in the previous subsection. It is still to understand, however, how these four terms form a balance of forces in the ice and how HD affects the balance. The balance of forces is first studied by reexamining the relative importance in Fig. 11. Thereafter, the variation of the balance in space and time is studied.

4.2.1. Balance of forces: averages

The left graph in Fig. 11 was computed with the proposed hydrodyamic model while the graph on the right was computed with its hydrostatic version, i.e. by disabling p_{HD} and p_{NLHD}. The dotted vertical lines indicate the transition velocity $V_{s \to d}$. Interactions with an ice velocity $V_{ice} < V_{s \to d}$ are classified as quasi-static while those with $V_{ice} > V_{s \to d}$ are classified as dynamic. The transition velocity is studied in Subsection 4.3.

First, consider the hydrodynamic model shown in the left graph. At the ice velocity $V_{ice} = 0$ the balance is mainly between bending and p_{HS}. As V_{ice} increases, the importance of p_{HS} quickly reduces while the importance of p_{HD}, i.e. the inertia of the fluid, increases. In the dynamic regime, the balance is mainly between p_{HD} and bending. Together they account for nearly the complete force balance. The inertia of the ice plays only a minor role, contributing up to 10% at high velocities.

Next, consider the hydrostatic model shown on the right. Although the graph appears different, the trends are actually similar. At low velocities bending is again balanced by p_{HS} and at high velocities, it is again balanced by inertia. However, as the inertia of the fluid is not accounted for, bending is now balanced by the inertia of the ice. In addition, the transition from quasi-static to dynamic occurs at a much higher velocity, 0.275 m/s compared to 0.07 m/s for the hydrodynamic model. From this, it can be concluded that p_{HD} adds a significant amount of inertia to the ice.

4.2.2. Balance of forces: temporal and spatial variation

The balance of pressure is studied again but now as a function of space and time. In the previous subsection two nonlinear terms, namely p_{NLHD} and axial compression were found to be insignificant. The only remaining nonlinearity is the contact model which is piece-wise linear in time. Despite the presence of the latter nonlinearity, all four significant forces show to be almost perfectly proportional to the ice velocity. This interesting property was also taken advantage of by Wang and Poh (2017) with their Rapid Analysis Strategy.

The proportionality of the four significant forces to the ice velocity allows them to be visualized for a range of ice velocities in a single figure. This is done in Fig. 12, which shows the dependence of the normalized by the ice velocity forces on time. For each ice velocity, the graphs are valid until the time t_{fail} at which failure of the ice occurs. The relation between t_{fail} and the ice velocity is shown in Fig. 13.

The response of the hydrodynamic model is shown in Fig. 12 on the left. Initially, the balance is between bending and inertia. The inertia of the fluid contributes significantly more, up to ten times as much as the inertia of the ice. p_{HS} does not contribute during the transient phase of the interaction and is only relevant in the steady-state regime, in which the normalized forces increase quasi-linearly in time. It is interesting to note that the bending stresses have a local maximum in the transient interaction phase. The maximum is followed by a local minimum as the system transitions into the steady-state regime. Similarly, p_{HD} also peaks during the transient interaction phase and then slowly decays back to zero, indicating that the action p_{HD} is of the added damping type. This effective damping is due to the energy being radiated in the form of flexural-gravity waves.

Comparing the graphs of the hydrostatic (the right part of Fig. 12) and hydrodynamic model shows markedly different behavior. Although the graphs of the hydrostatic model contain some noise introduced at the transient phase of the interaction, the trends are very clear. The
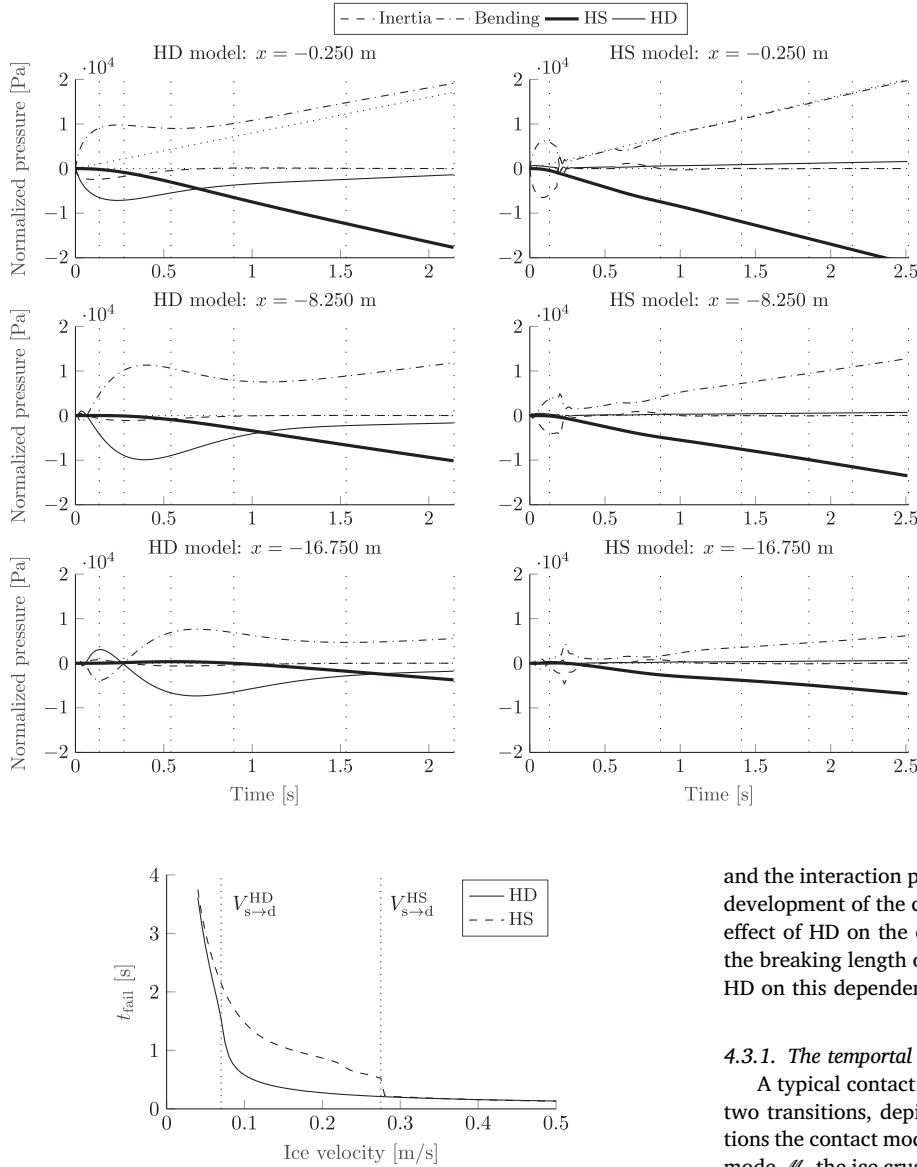
Fig. 12. The various pressures that act on the ice at three location in the ice normalized by the ice velocity. A zero-line and the static bending pressure are included for reference with the dotted sloped lines. The vertical loosely dotted lines indicate the failure time t_{fail} at the following ice velocities (from left to right): 0.5, 0.2, 0.1, 0.08, 0.07 and 0.06 m/s.

Fig. 13. The failure time t_{fail} of the hydrodynamic (HD) model and the hydrostatic (HS) model. The vertical dotted lines indicate the transition velocity $V_{s \to d}$ of both models.

transient phase of the hydrodynamic model lasts significantly longer and the bending stresses experienced during this phase are also much larger. Both effects imply that p_{HD} adds a significant amount of inertia to the ice. The drop in the bending stress after the peak is also more abrupt for the hydrostatic model.

Lastly, two observations can be made from the times of failure t_{fail} of both models shown in Fig. 13. Firstly, as V_{ice} increases, the duration of the interaction decreases, meaning that the role of the transient interaction phase becomes more and more significant as the ice velocity increases. This is in agreement with the trends seen in Fig. 11. Secondly, as the bending stresses generated during the transient interaction phase are much lower for the hydrostatic model, even at high ice velocities the ice fails statically.

4.3. The relation between contact force and breaking length

Understanding the relation between the temporal development of the contact force and velocity-dependence of the breaking length requires a thorough understanding of the evolution of the contact force

and the interaction process. Therefore, a detailed study on the temporal development of the contact force is carried out first. Following this, the effect of HD on the contact force is studied. Lastly, the dependence of the breaking length on the ice velocity is studied as well as the effect of HD on this dependency.

4.3.1. The temporal development of the contact force

A typical contact force profile is shown in Fig. 14. This figure shows two transitions, depicted by the dashed vertical lines. At these transitions the contact model switches between its two modes. In the crushing mode $\mathcal{M}_c$ the ice crushes and in the sliding mode $\mathcal{M}_s$ the ice slides along the structure. Consequently, the magnitude of the contact force $F_{ct}(t)$ is defined as:

$$F_{ct}(t) = \begin{cases} \sigma_c A_{ct}(t) & \text{when crushing } (\mathcal{M}_c) \\ \sigma_{ct}(t) A_{ct}^* & \text{when sliding } (\mathcal{M}_s) \end{cases} \tag{44}$$

where $F_{ct}(t) = \sqrt{(F_{ct,x}(t))^2 + (F_{ct,z}(t))^2}$, σ_c is the representative crushing
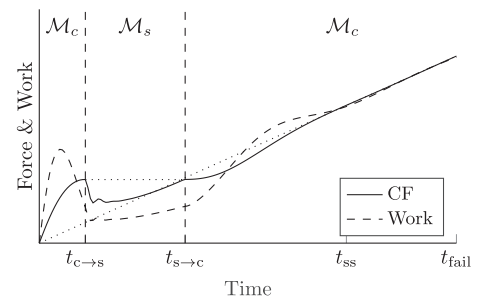

Fig. 14. An illustration of how the contact force (CF), the solid curve, develops during a typical interaction. The work done by the contact is shown by the dashed curve. Both signals are normalized. The contact force based on a static equilibrium is depicted with the dotted diagonal line. The dashed vertical lines delimit the two modes of the contact model.
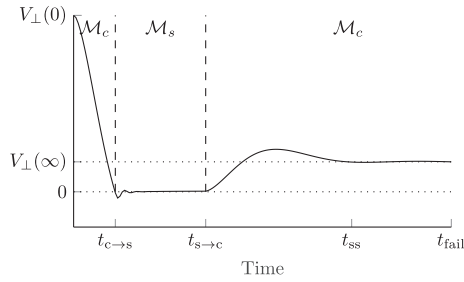
Fig. 15. The speed at which the ice penetrates into the structure $V_{pen}(t)$ during a typical interaction. The steady-state penetration speed and a zero line are included for reference. The dashed vertical lines delimit the two modes of the contact model.

Fig. 16. The contact force and $V_\perp$ for the hydrostatic (dashed) and hydrodynamic model (solid). The dotted line on the left shows the static contact force. On the right a zero line and $V_\perp(\infty)$ are included for reference. V_{ice} was set to 0.05 m/s for this figure.

strength of the ice, $A_{ct}(t)$ is the variable contact area between ice and structure in the crushing mode, $\sigma_{ct}(t)$ is the variable contact stress while sliding and A_{ct}^* is the fixed contact area in sliding.

At the start of the interaction the contact area is very small which means that even a relatively small contact force causes crushing of the ice. During the transient interaction phase, a large amount of work has to be performed to align the ice's tip-velocity with the structure's hull. This work is performed by the contact force during the transient phase and results in a peak in the force ($t = t_{c \to s}$ om Fig. 14). Therefore, most of this work transfers to the kinetic energy in both ice and fluid. Once the ice tip velocity has aligned itself with the structure, the required work drops and consequently the contact force drops as well. After this moment in time, most of the work done by the contact force is used to increase the potential energy of the ice and fluid, namely by increasing the curvature of the ice (bending) and by increasing the hydrostatic draft of the ice.

The alignment of the tip with the structure is illustrated in Fig. 15. This figure shows the normal to the structure component $V_\perp(t)$ of the velocity of the tip of the ice. The interaction begins with $V_\perp(t)$ dictated by the initial conditions $V_\perp(0) = V_{ice} \sin(\theta)$. Immediately after, $V_\perp(t)$ experiences a rapid drop and reaches zero at $t_{c \to s}$ as can be seen in Fig. 14. At this moment the contact force starts to decrease. Consequently, the contact model has to transition into the sliding mode $\mathcal{M}_s$. While in this mode the contact area remains constant at $A_{ct}^* = A_{ct}(t_{c \to s})$ and the contact stress $\sigma_{ct}(t)$ becomes variable with $\sigma_{ct}(t) \in [0, \sigma_c]$. $\sigma_{ct}(t)$ is ideally computed using Lagrangian Multipliers. However, this approach gave numerical issues. To avoid these, a very stiff contact spring was used to approximate a rigid contact. This finite stiffness results in $V_\perp(t)$ becoming slightly negative just after $t_{c \to s}$.

The contact model remains in $\mathcal{M}_s$ until the contact stress becomes larger than σ_c. This happens at $t_{s \to c}$ and results in a second transient stage. After this the ice transitions into the steady-state regime. It is important to note that $V_\perp(t)$ converges to a constant value rather than to zero. This is because in the steady-state regime the ice continuously crushes at a constant rate. This requires the contact force to grow linearly in time in order to balance with the increasing bending and hydrostatic forces, as shown in Fig. 14.

4.3.2. HD influence on the contact force

Fig. 16 shows a comparison between the contact force F_{ct} predicted by the hydrostatic and the hydrodynamic model. On the left, the contact force of both models is shown and on the right their $V_\perp(t)$.

Both graphs show that HD greatly increases the resistance provided by the water against the ice bending. Analyzing the contact force shown in Fig. 16, this is apparent in two ways. Firstly, the force peak during the transient interaction phase is greatly increased by HD, which is indicative of increased inertia. Secondly, the ensuing transition to the steady-state equilibrium is much slower for the HD model, which is indicative of increased damping. Both effects can also be observed in Figs. 11 and 12.
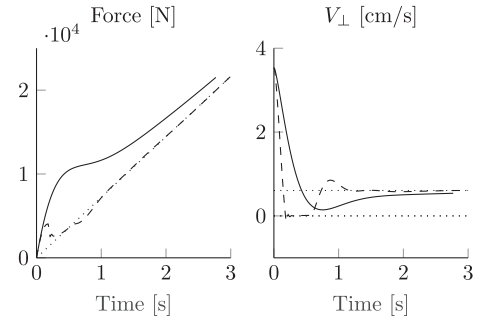
Looking at $V_\perp$ similar conclusions can be drawn. $V_\perp$ of the hydrostatic model overshoots the static equilibrium and indicates sliding ($\mathcal{M}_s$ regime) while $t \in [0.18, 0.57]$ s. $V_\perp$ of the HD model changes much slower, again indicative of increased inertia, and never enters $\mathcal{M}_s$. Within the HD model, $V_\perp$ does overshoots $V_\perp(\infty)$ but does so only a little. This is similar to a system with significant, but less than critical, damping. This is in stark contrast to the hydrostatic model that exhibits a lightly damped response.

To conclude, HD adds a significant amount of resistance to the ice in the form of added mass and damping. This increases the contact force during the transient interaction phase and results in a highly damped behavior of the ice.

4.3.3. The relation between breaking length and contact force

Next, the breaking length is analyzed in order to understand its relation with the temporal development of the contact force studied previously. Special attention is again given to the effect of HD on this relation. The breaking length as a function of ice velocity is shown in Fig. 17 for both the hydrodynamic and hydrostatic model.

Fig. 17 reveals three interesting features. Firstly, it is clear that for both models the breaking length as a function of ice velocity behaves distinctly different at lower and higher ice velocities. The transition between the two regimes occurs at the transition velocity $V_{s \to d}$, indicated in Fig. 17 for each model with the vertical dotted line. Secondly, the figure shows that $V_{s \to d} = V_{s \to d}^{HD}$ of the hydrodynamic model is much smaller than $V_{s \to d} = V_{s \to d}^{HS}$ of the hydrostatic model. Lastly, the breaking length changes very abruptly at velocities close to the transition velocity $V_{s \to d}$. These three features are explained next.

Firstly, in order to understand the existence of the two regimes, consider that the initial peaks in the contact forces of both models, as seen in Fig. 16 on the left, are caused by the initial impact between ice and structure. The magnitude of both peaks scales with the ice velocity V_{ice}. Therefore, it makes sense for a certain velocity $V_{s \to d}$ to exist, above which the impact is so strong that the ice fails during the impact. These
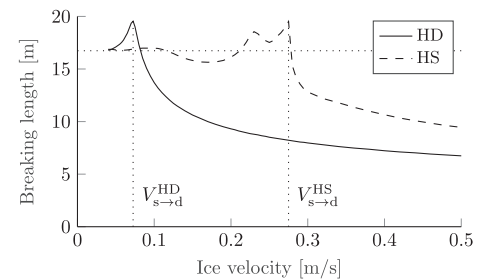

Fig. 17. The breaking length as a function of ice velocity for the hydrodynamic and hydrostatic (HS) model. The dotted line is the static breaking length computed with Eq. (20). The dotted vertical lines indicate $V_{s \to d}$ of each model.

interactions, for which $V_{ice} > V_{s\to d}$, are classified as dynamic. The magnitude of the peak in the contact force continues to grow as V_{ice} increases which causes the ice to fail earlier and closer to the contact point. This can be observed in Fig. 17 for both model.

Alternatively, if the impact is not strong enough the ice will survive the peak force that occurs during the transient stage of the interaction ($t < t_{c\to s}$ in Fig. 14). This occurs if $V_{ice} < V_{s\to d}$. In this regime, the ice will fail with a breaking length that is approximately equal to the static breaking length. The static breaking length is given by Eq. (A5) and is indicated in Fig. 17 with the horizontal dotted line.

Secondly, it is important to note that $V_{s\to d}^{HD}$ is much lower than $V_{s\to d}^{HS}$. The left graph in Fig. 16 shows that the initial peak in the contact force of the hydrodynamic model is significantly larger than the same peak of the hydrostatic model for any given ice velocity. Consequently, the hydrodynamic model predicts dynamic failure of the ice at much lower velocities.

Lastly, the breaking length of both models changes abruptly at velocity close to the transition velocity $V_{s\to d}$, i.e. while transitioning from the quasi-static to the dynamic regime. This behavior will first be explained for the hydrostatic model. Fig. 14, which corresponds to the hydrostatic model, and the left graph of Fig. 16 both show that starting from $t_{c\to s}$ and ending at $t_{s\to c}$ the contact force is lower than during the transient interaction phase. The reduction of the contact force during this relaxation period results in a similar drop in the axial stress due to bending (the contribution of the axial compression in Eq. (7) is constant in space), see Fig. 18. During the relaxation period the ice cannot fail as the maximum bending moment in the ice is lower than experienced previously. Consequently, if the ice survives the transient interaction phase, the duration of the interaction will increase by approximately the duration of the relaxation period. This behavior can be observed in Fig. 13 as a jump in the failure time t_{fail} around $V_{s\to d}^{HS}$. Fig. 18 shows that after the relaxation period the stresses in the ice are very close to their steady-state values. Because of this the ice will fail with a breaking length that is very close to the static one. Therefore, whether the ice survives the transient interaction phase has drastic effects on the breaking length of the hydrostatic model. This behavior is also reflected in Fig. 17 as the breaking length decreases abruptly by about four meters at $V_{s\to d}^{HS}$.

The abrupt behavior of the breaking length at ice velocities close to $V_{s\to d}^{HD}$ of the hydrodynamic model is analyzed next. Fig. 19 shows that the stresses predicted by the hydrodynamic model always increase in time. However, between approximately 0.5 and 1.5 s, the stresses grow at a very slow pace. This corresponds to the period wherein $0 < V_\perp(t) < V_\perp(\infty)$ in Fig. 16 on the right. The reduced growth rate of the contact force makes it easier for the ice to survive this quasi-relation period. This is reflected in Fig. 13 by the rapid reduction of the interaction time around $V_{s\to d}^{HD}$ and in Fig. 17 by the rapid decrease of the breaking length after $V_{s\to d}^{HD}$.
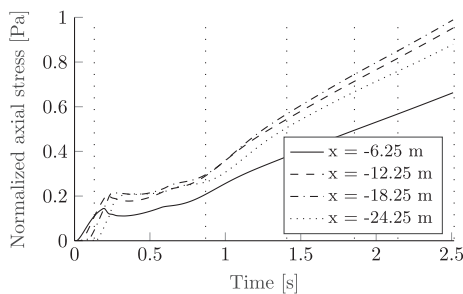

Fig. 18. The axial stress due to bending of the hydrostatic model normalized by the flexural yield stress σ_{fl} as a function of time at four locations. For this figure $V_{ice} = 0.06$ m/s. The vertical loosely dotted lines indicate the failure time t_{fail} at the following ice velocities (from left to right): 0.5, 0.2, 0.1, 0.08, 0.07 and 0.06 m/s.
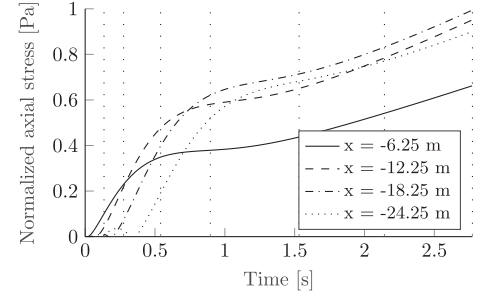

Fig. 19. The axial stress of the hydrodynamic model normalized by the flexural yield stress σ_{fl} as a function of time at four locations. For this figure $V_{ice} = 0.05$ m/s. The vertical dotted lines indicate the failure time t_{fail} at the following ice velocities (from left to right): 0.5, 0.2, 0.1, 0.08, 0.07, 0.06 and 0.05 m/s.

4.4. Limitation of the hydrostatic model

Based on the above discussion it is clear that the results of the hydrodynamic and hydrostatic model start to differ, both qualitatively and quantitatively, from $V_{ice} \approx V_{s\to d}^{HD}$. The two main characteristics of ISI, namely the breaking length and the maximum contact force, as predicted by both models, are compared in order to assess the validity range of the hydrostatic model.

The hydrostatic model starts to predict the breaking lengths wrongly after approximately $0.6 V_{s\to d}^{HD}$, see Fig. 17. With the parameter set used, $V_{s\to d}^{HD}$ is approximately 0.0725 m/s and so the hydrostatic model correctly predicts the breaking length up to approximately 0.05 m/s. For interactions with a higher ice velocities, the relative error in the predicted breaking length can be as much as 100%.

The maximum contact force within $t \in [0, t_{fail}]$ of both models is compared in Fig. 20. The predictions of both models again start to deviate around $0.6 V_{s\to d}^{HD}$ with the relative error increasing up to 40%.

From these two comparisons it can be concluded that if a hydrostatic model is used to predict the breaking length or maximum contact force during ISI, the range of ice velocities wherein the predictions are valid is very limited. An approximate upper bound for the maximum ice velocity of the hydrostatic model is $0.6 V_{s\to d}^{HD}$.

5. Sensitivity study

The sensitivity of the model to changes in the parameter set is studied next. The focus is mainly on how $V_{s\to d}$ is affected by these changes as the applicability of the hydrostatic model is directly linked to $V_{s\to d}$.

The parameters that have a large variance are the ice thickness h, Young's modulus E, flexural strength σ_{fl}, crushing strength σ_c the water depth H and the hull angle θ. The effect of the simplified vessel model in Fig. 8 is also studied. Lastly, the sensitivity of the model to the number of modes N_{modes} is studied.
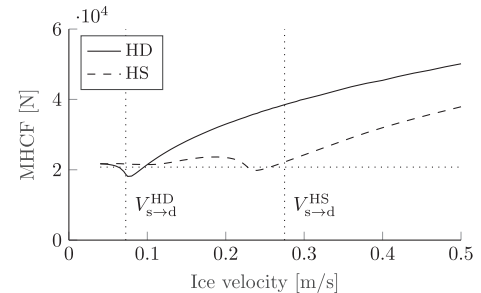

Fig. 20. The maximum horizontal contact force (MHCF) of both models. The static force is included for reference.

The sensitivity of the system to changes in the listed parameters is assessed using the following figures for the parameters: $h = \{0.5, 2\}$ m, $E = \{2.5 \times 10^9, 10^{10}\}$ Pa, $\sigma_{fl} = \{2.5 \times 10^5, 10^6\}$ Pa, $\sigma_c = \{3 \times 10^5, 1.2 \times 10^6\}$ Pa, $H = \{50, 200\}$ m and $\theta = \{30, 60\}°$.

The default values for the transition velocity $V_{s \to d}$ are: $V_{s \to d}^{HD} = 0.0725$ m/s and $V_{s \to d}^{HS} = 0.275$ m/s.

5.1. Variations in physical parameters

5.1.1. Ice thickness

Halving h to 0.5 m causes the hydrodynamic model to be in the sliding mode $\mathcal{M}_s$ for a total of 0.2 s (compared to 0.45 s for the hydrostatic model) and reduces $V_{s \to d}^{HD}$ to 0.065 m/s. Doubling h to 2 m increases $V_{s \to d}^{HD}$ to 0.08 m/s.

5.1.2. Young's modulus

$V_{s \to d}$ is relatively sensitive to changes in E. Halving E to 2.5×10^9 Pa increases $V_{s \to d}^{HD}$ to 0.11 m/s and $V_{s \to d}^{HS}$ to 0.38 m/s. When E is doubled to 10^{10} Pa, $V_{s \to d}$ decreases considerably for both models, to 0.045 m/s and 0.19 m/s respectively.

5.1.3. Flexural strength

σ_{fl} has a strong effect on $V_{s \to d}$. When halved to 2.5×10^5 Pa, $V_{s \to d}^{HD}$ lowers to roughly 0.03 m/s and $V_{s \to d}^{HS}$ to 0.135 m/s. Doubling σ_{fl} to 10^6 Pa has the opposite effect, increasing the $V_{s \to d}^{HD}$ to about 0.145 m/s and $V_{s \to d}^{HS}$ to > 0.5 m/s.

5.1.4. Crushing strength

When σ_c is doubled to 1.2×10^6 the hydrodynamic model is in the sliding mode $\mathcal{M}_s$ for a total of 0.45 s, compared to 0.55 s for the hydrostatic model. The overall contact force increases while the overall interaction quickens. Halving σ_c has the opposite effect. It appears that both effects cancel each other out as neither the breaking length nor $V_{s \to d}$ is significantly affected by changes in σ_c.

5.1.5. Water depth

The influence of H is negligible. Values as low as 30 m and as high as 200 m were tested but these did not affect the breaking length, nor $V_{s \to d}$.

5.1.6. Hull angle

θ affects $V_\perp(0) = V_{ice} \sin(\theta)$ as well as the ratio between the horizontal and vertical contact forces. Increasing θ to 60° lowers $V_{s \to d}^{HD}$ to 0.045 m/s and $V_{s \to d}^{HS}$ to 0.16 m/s. The contribution of the axial compression to the dynamic equilibrium of the ice sheet studied in Subsection 4.1 is not significantly affected by the steeper hull angle. Lowering θ to 30° increases $V_{s \to d}^{HD}$ to 0.12 m/s and $V_{s \to d}^{HS}$ to 0.46 m/s and causes the HD model to enter the sliding mode $\mathcal{M}_s$ for a total of 0.3 s compared to 0.55 s for the hydrostatic model.

5.2. Variation in numerical parameters and in modeling assumptions

5.2.1. Number of modes

The Green's functions used in 2.2 used to describe the response of the system in the ice-covered region are a superposition of the infinite modes of the system. The infinite number of modes was truncated at N_k. The truncation introduces an error that manifests itself at $x = 0$ as a discontinuity in the displacements and pressure of the fluid along the entire water column. The discontinuity is largest just below the surface. The two regions merge as the number of modes increases.

N_k is gradually lowered to study how it affects the ISI. While values of N_k as low as ten have only minor effects on the breaking length and maximum contact force and their dependence on the ice velocity, such a low number of modes causes very large discontinuities in the displacements and pressure of the fluid along the interface at $x = 0$.

5.2.2. Modeling the structure

Lastly, the effect of reducing the infinite problem shown in Fig. 1 to the semi-infinite problem shown in Fig. 8 is studied. This change has only a minor effect, reducing $V_{s \to d}^{HD}$ from 0.0725 m/s to 0.05 m/s. The average breaking length is lowered by approximately 7%. The effect on the maximum contact force is just as minor.

6. Discussion

6.1. Stochastic nature of the breaking length

When analyzing the breaking length it is common to present it as a deterministic value, similar to Fig. 17. However, even the deterministic models used in this paper underline the stochastic nature of the breaking length.

Thus far in this paper, the breaking length has been defined as the cross-section of the ice plate at which the axial stress first exceeds the flexural strength of the ice. However, this definition does not account for the fact that at the moment the ice fails, a large segment of the ice is very close to failure. This was also noted in Valanto (1992). If in this segment a local defect is present, for instance, a lower ice thickness, the resulting stress-peak could cause the ice to fail at the location of the defect rather than at the location predicted by a homogeneous model.

The sensitivity of the breaking length to such defects is shown in Fig. 21. The sensitivity is quantified using the axial stress, see Eq. (7), at the time of failure t_{fail} normalized by the flexural yield stress: $|\sigma_{max}(x, t_f)/\sigma_{fl}|$. The shaded regions indicate the possible breaking lengths that correspond to a 1% and 10% variation in $|\sigma_{max}(x, t_f)/\sigma_{fl}|$.

Given that ice is very inhomogeneous material (Timco and Weeks, 2010), spatial variations in the ice thickness h, Young's modulus E or flexural yield stress σ_{fl} of several percentages are more than realistic. Fig. 21 shows that even such small variations can have a large effect on the breaking length. With a 1% variation in, for instance, the Young's modulus, the breaking length can change by as much as 10%. When the variation is further increased to 10%, the breaking length can change by as much as 30%. Fig. 21 thus shows that even a deterministic model underlines the stochastic nature of the breaking length. Therefore, presenting the breaking length as a deterministic property does not seem to be desirable.

6.2. Single- versus dual-mode contact model

The contact model used in this paper has two modes: a crushing mode and a sliding mode. The sliding mode is triggered at $t_{c \to s}$ (see Fig. 14) when $V_\perp$ becomes zero (see Fig. 15) and assures that the ice slides along the structure without crushing.

However, it is not uncommon for ISI models to use a single-mode model that only accounts for crushing. Such a model will work fine as long as $V_\perp > 0$. However, in this work, this assumption would not have
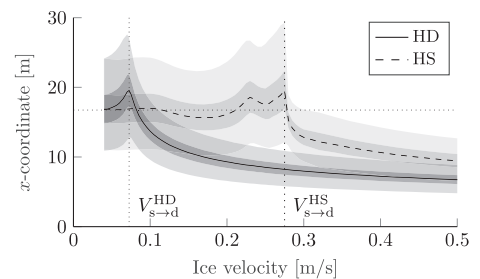

Fig. 21. The breaking length of the hydrodynamic model (HD) and hydrostatic model (HS). The dark gray shading indicates the possible breaking lengths due to a 1% variation in the normalized axial stress and the light gray shading a variation of 10%. The horizontal dotted line indicates the static breaking length computed with Eq. (20).
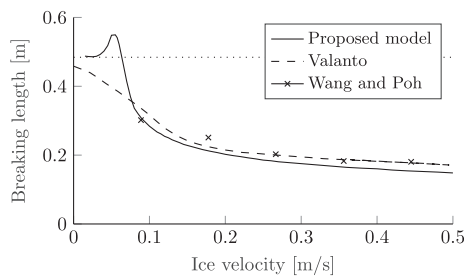
Fig. 22. The breaking length as a function of the ice velocity. The horizontal dotted line is the static breaking length computed with Eq. (20).

been valid. Fig. 16 shows that the hydrostatic model enters the sliding mode and certain parameters choices also cause the hydrodynamic model to enter the sliding mode, see Section 5.1. Therefore, a single-mode contact model would not suffice for the studies done in this paper. If such a contact model were used it would affect the dependence of the breaking length on the ice velocity around $V_{s \to d}$ and the contact force after $t_{c \to s}$. In general, when a single-mode contact model is used in an ISI model, the underlying assumption that $V_\perp$ is assumed to be larger than zero should be more explicitly mentioned and the validity of this assumption should be asserted throughout the study.

6.3. Effect of the solution method

To the authors' knowledge, only two other works have studied ISI in 2D using a numerical model that includes hydrodynamics: Valanto (1992) and Wang and Poh (2017). The breaking length as a function of ice velocity as predicted by all three models is shown in Fig. 22. At high velocities, all three models predict comparable breaking lengths. At low velocities, the model introduced in this paper predicts a quasi-static regime. Valanto (1992) does not predict a quasi-static regime in the dependence of the breaking length of the ice velocity and Wang and Poh (2017) did not do any calculations in this regime.

It can shown that by introducing a large amount of damping to the hydrostatic model, a similar velocity-dependence of the breaking length as predicted by Valanto (1992) can be obtained. For such a model $V_\perp(t) > V_\perp(\infty)$ and, in the course of ISI, $V_\perp(t)$ decreases monotonically to its steady-state value. This kind of behavior of $V_\perp$ can also be seen in Wang and Poh (2017). Therefore, it can be concluded that both other models predict a stronger hydrodynamic effect than the model introduced in this paper.

This difference is likely to be caused by the different assumptions and solution method adopted by the models. Valanto (1992) uses Finite Difference for the dicretization of both the fluid and the ice and considers the steady-state velocity of the fluid around the structure. Wang and Poh (2017) use the Finite Element Method for the discretization, adopt a single-stage contact model and do not include the steady-state velocity.

The model in this paper thus differs in three ways from the two cited models. Firstly, the effect of a single stage contact model versus a two-stage contact model only affects the behavior near the transition velocity $V_{s \to d}$, as explained in Subsection 6.2, and therefore cannot explain the different results. Secondly, the effect of the steady-state velocity of the fluid around the structure can be inferred by comparing Wang and Poh (2017) and Valanto (1992). As there is still a discrepancy between the herein proposed model and Wang and Poh (2017), this can only explain part of the difference in the results. The adopted solution method thus appears to be the most likely source of the discrepancy. However, as the available data is lacking and both models are not publicly available, a detailed study on the effect of the solution method is not possible.

7. Conclusion

In this paper, the bending failure of level ice caused by the interaction

with a downward sloping structure was studied. The focus was on the effect of hydrodynamics (HD) on the interaction. This study was done by comparing the results of a model that includes both hydrostatics and HD with one that only includes hydrostatics. The conclusions of this study are presented next.

7.1. The factors of influence for ISI

In this work, seven forces were accounted for in the dynamic equilibrium of the ice. The contribution of the rotational inertia, the axial compression and the nonlinear hydrodynamic pressure p_{NLHD} to the dynamic equilibrium were found to be < 1%. These three terms can thus be ignored without significantly affecting the results of an ISI model. Being able to ignore the axial compression and p_{NLHD} greatly simplifies the modeling of ISI as it removes all sources of spatial nonlinearity. Note that only the nonlinear contribution of the axial compression to the dynamic equilibrium of the ice can be ignored. Its linear contribution to the axial stresses was not studied and so no conclusion can be drawn regarding this.

The remaining four terms are essential for an accurate description of ISI. These terms, listed in the order of importance, are: bending of the ice, the linear hydrodynamic pressure p_{HD}, hydrostatic pressure p_{HS} and the inertia of the ice.

The hydrodynamic effect is given by the combined effect of p_{HD} and p_{NLHD}. The relative importance of these two terms had not been studied before. However, from this work, it can be concluded that the entirety of the hydrodynamic effect can be attributed to the linear hydrodynamic pressure.

7.2. The relation between the contact force and the breaking length

A detailed study on the relation between the velocity-dependency of the breaking length and the temporal development of the contact force revealed two interesting features.

Firstly, the velocity dependence of the breaking length has two regimes that are separated by the transition velocity $V_{s \to d}$: a quasi-static regime when the ice velocity $V_{ice} < V_{s \to d}$ and a dynamic regime when $V_{ice} > V_{s \to d}$. In the dynamic regime, the ice fails during the transient interaction phase. The resulting breaking length is significantly smaller than the static breaking length and decreases as the ice velocity increases. Alternatively, if the ice does not fail in the transient regime, it often reaches the steady-state regime an will fail with a breaking length that is close to the static breaking length.

Secondly, the transition velocity of the hydrodynamic model $V_{s \to d}^{HD}$ is much lower than the transition velocity of the hydrostatic model $V_{s \to d}^{HS}$: 0.0725 m/s compared to 0.275 m/s. $V_{s \to d}^{HD}$ decreases as the Young's modulus or hull angle is increased and increases as the flexural strength of the ice is increased. Other parameters such as the thickness, crushing strength and water depth have a negligible effect on the transition velocity.

7.3. The balance of forces

For interactions with an ice velocity V_{ice} that is below the transition velocity $V_{s \to d}$, bending is balanced by hydrostatics. For interactions with $V_{ice} > V_{s \to d}$ bending is balanced by inertia of the fluid and the inertia of the ice. The contribution of the inertia of the fluid, i.e. the contribution of the hydrodynamic pressure, is on average four to ten times bigger than that of the inertia of the ice.

7.4. The limitations of a hydrostatic model

The contact force and breaking length predicted by the hydrostatic model start to diverge rapidly from those predicted by the hydrodynamic model when $V_{ice} \approx 0.6 V_{s \to d}$. The error ranges from 30% to 100%. As such it is not recommended to use hydrostatic models for interactions with ice velocities above approximately 0.05 m/s.

7.5. The importance of the open water region

Truncating the computation domain from infinite to semi-infinite had only minor effects on the breaking length and the contact force. This shows that the energy loss due to the radiation of surface waves into the open water region has only minor effects on ISI.

7.6. The stochastic nature of the breaking length

Lastly, when the ice fails, a relatively large segment of the ice is close to failure. Defects in the ice can amplify the stresses in this

segment and can cause the ice to fail at the defect rather than at the expected location. This can easily cause the breaking length to vary by 10% to 30%.

Appendix A. Static breaking length

The contact model used in this paper accounts for the tip moment and this has a minor effect on the static breaking length. An analytical expression for the static breaking length is derived next.

In the static limit the equation of motion of the ice given by Eq. (4) reduces to:

$$\frac{EI}{1-\nu^2}w''''(x) + \rho_w g w(x) = 0 \qquad \forall \ x \in (-\infty, 0] \tag{A.1}$$

The general solution to this ODE that accounts for the proper behavior at $x \rightarrow -\infty$ is:

$$w(x) = c_1 \exp(r_1 x) + c_2 \exp(r_2 x) \tag{A.2}$$

where c_1 and c_2 are unknown integration constants, $r_1 = (-1-i)\sqrt{2}l/2$ and $r_2 = (-1+i)\sqrt{2}l/2$ with $l = \sqrt[4]{\delta}$, where δ is defined in Eq. (11). To complete the problem statement two boundary conditions are needed. The boundary conditions account for the contact force and moments that act on the edge of the plate:

$$\frac{EI}{1-\nu^2}w'''(0) = \sigma_{cr}(V_{ice}t\tan(\theta) - w(0))\cos(\theta) \tag{A.3}$$

$$\frac{EI}{1-\nu^2}w''(0) = -h/2\sigma_{cr}(V_{ice}t\tan(\theta) - w(0))\sin(\theta) \tag{A.4}$$

The contact force is assumed to act at the top of the cross-section of the ice. The arm of the horizontal component of the contact force with respect to the neutral axis is thus $h/2$.

These two boundary conditions can be used to find expressions for the unknown constants c_1 and c_2. The breaking length can be found by determining the location where the bending stress, given by the first term in Eq. (7), is maximum. This results in the following expression for the static breaking length:

$$x_{bl} = \sqrt{2}\,l\,a\tan\left(\frac{\sqrt{2}l}{\sqrt{2}l - h\tan(\theta)}\right) \tag{A.5}$$

References

Alawneh, S., Dragt, R., Peters, D., Daley, C., Bruneau, S., 2015. Hyper-real-time ice simulation and modeling using GPGPU. IEEE Trans. Comput. 64 (12), 3475–3487. ISSN 00189340. https://doi.org/10.1109/TC.2015.2409861.

Aprile, A., Benedetti, A., Trombetti, T.L., 1994. On non-linear dynamic analysis in the frequency domain: algorithms and applications. Earthq. Eng. Struct. Dyn. 23 (4), 363–388. ISSN 00988847. https://doi.org/10.1002/eqe.4290230403.

Bird, K.J., Charpentier, R.R., Gautier, D.L., Houseknecht, D.W., Klett, T.R., Pitman, J.K., Moore, T.E., Schenk, C.J., Tennyson, M.E., Wandrey, C.J., 2008. Circum-Arctic Resource Appraisal: Estimates of Undiscovered Oil and Gas North of the Arctic Circle. USGS Fact Sheet 2008-3049. pp. 1–4. ISSN 2327-6932. USGSFactSheet2008-3049.

Dempsey, J.P., Zhao, Z.G., 1993. Elastohydrodynamic sheet to forced sub-surface uplift. J. Mech. Phys. Solids 41 (3), 487–506.

Jensen, F.B., Kuperman, W.A., Porter, M.B., Schmidt, H., 2011. Computational Ocean Acoustics. Springer, New York, NY ISBN 978-1-4419-8677-1. https://doi.org/10.1007/978-1-4419-8678-8.

Keijdener, C., Metrikine, A.V., 2014. The effect of ice velocity on the breaking length of level ice failing in downward bending. In: Proceedings of 22nd IAHR International Symposium on Ice, http://dx.doi.org/10.3850/978-981-09-0750-11262.

Keijdener, C., de Oliveira Barbosa, J.M., Metrikine, A.V., 2017. The influence of level ice on the frequency domain response of floaters. Cold Reg. Sci. Technol. 143 (July), 112–125. http://dx.doi.org/10.1016/j.coldregions.201709.004.

Konno, A., Nakane, A., Kanamori, S., 2013. Validation of numerical estimation of brash ice channel resistance with model test. In: Proceedings of the 22nd International Conference on Port and Ocean Engineering under Arctic Conditions. vol. 143.

Lu, W., Lubbad, R., Høyland, K., Løset, S., 2014. Physical model and theoretical model study of level ice and wide sloping structure interactions. Cold Reg. Sci. Technol. 101, 40–72. May. https://doi.org/10.1016/j.coldregions.2014.01.007.

Lubbad, R., Loset, S., 2011. A numerical model for real-time simulation of ship-ice interaction. Cold Reg. Sci. Technol. 65 (2), 111–127. ISSN 0165232X. https://doi.org/10.1016/j.coldregions.2010.09.004.

Metrikin, I., Gürtner, A., Bonnemaire, B., Tan, X., Fredriksen, A., Sapelnikov, D., 2015. SIBIS: A numerical environment for simulating offshore operations in discontinuous ice. In: Proceedings of the 23rd International Conference on Port and Ocean Engineering under Arctic Conditions, Trondheim.

Paavilainen, J., Tuhkuri, J., Polojärvi, A., 2009. 2D combined finite-discrete element method to model multi-fracture of beam structures. Eng. Comput. 26 (6), 578–598. ISSN 0264-4401. https://doi.org/10.1108/02644400910975397.

Sayed, M., Kubat, I., Watson, D., Wright, B., Gash, R., Millan, J., 2015. Simulations of the station keeping of drillships under changing direction of ice movement (OTC 25565). In: Arctic Technology Conference, ATC'15, pp. 1–15. http://dx.doi.org/10.4043/25565-MS.

Stoker, J.J., 1992. Water Waves. John Wiley & Sons, Inc, Hoboken, NJ, USA Jan. https://doi.org/10.1002/9781118033159.

Su, B., Riska, K., Moan, T., 2010. A numerical method for the prediction of ship performance in level ice. Cold Reg. Sci. Technol. 60 (3), 177–188. ISSN 0165232X. https://doi.org/10.1016/j.coldregions.2009.11.006.

Timco, G.W., Weeks, W.F., 2010. A review of the engineering properties of sea ice. Cold Reg. Sci. Technol. 60 (2), 107–129. ISSN 0165232X. https://doi.org/10.1016/j.coldregions.2009.10.003.

Valanto, P., 1992. The icebreaking problem in two dimensions: experiments and theory. J. Ship Res. 36 (4), 299–316.

Wang, Y., Poh, L.H., 2017. Velocity effect on the bending failure of ice sheets against wide sloping structures. J. Offshore Mech. Arctic Eng. 139 (6), 061501. ISSN 0892-7219. https://doi.org/10.1115/1.4036478.

Williams, T.D., Squire, V.A., 2008. The effect of submergence on wave scattering across a transition between two floating flexible plates. Wave Motion 45 (3), 361–379. ISSN 01652125. https://doi.org/10.1016/j.wavemoti.2007.07.003.

Zhao, Z.G., Dempsey, J.P., 1996. Planar forcing of floating ice sheets. Int. J. Solids Struct. 33 (1), 19–31.